

# Nanophotonics with Hybrid Nanostructures: New Phenomena and New Possibilities

Noor Eldabagh, Jessica Czarnecki, and Jonathan J. Foley IV\*

*Department of Chemistry, William Paterson University, 300 Pompton Road, Wayne, NJ,  
07470, USA*

E-mail: foleyj10@wpunj.edu

## Abstract

The optical response of materials as one or more of their dimensions approaches the nanoscale is marked by the onset of a number of remarkable and desirable phenomena. Metal nanoparticles can support resonant surface plasmon excitations, semiconductor nanoparticles (e.g. quantum dots) support excitonic resonances, and dielectric nanoparticles support a number of scattering resonances. Generally speaking, the precise resonant behavior in all these cases can be systematically tuned by changing the environment and the geometry of the nanoparticle without changing its material properties. This leads to a vibrant palette of optical behaviors for scientists to explore and apply to a variety of applications. This palette can be made more vibrant still by bringing together these various nano elements to form the menagerie of possible hybrid nanostructures, as the interaction between these elements can often give rise to surprising new and emergent phenomena. The ultimate goal of the field of nanophotonics is to precisely control how optical energy and information flows at nanoscale and molecular scale dimensions, and to realize and dream up new applications for this exquisite control.

---

\*To whom correspondence should be addressed

This chapter introduces a variety of theoretical and computational approaches that can be used to elucidate the optical response of hybrid nanostructures. We examine how emergent phenomena can arise from purely electrodynamics effects in these structures, as well as how changes in material properties brought about by chemical and physical interactions between domains in hybrid nanostructures can give rise to emergent optical phenomena. We will discuss how these phenomena, and theoretical methodologies that can be used to study and predict these phenomena, may be brought to bear in designing novel structures that display exquisitely tuned optical properties. In particular, we will focus on the potential of using hybrid nanostructures with tailored optical properties for health applications. Control of optical energy and information flow at nanoscale and molecular dimensions can lead to concrete advances in a variety of health applications, for example, by enabling targeted illumination strategies for photothermal and photodynamic therapies, by advancing the sensitivity of diagnostic techniques, by advancing the resolution of imaging techniques, and by allowing the construction of devices that can act as *in vivo* optical systems. Additionally, control of optical energy and information flow can enhance our ability to probe complex biological systems so as to advance our basic understanding of therapeutic mechanisms.

The theory and phenomenology of the optical response of several metallic hybrid nanostructures will be discussed in detail. We will frame the intriguing optical properties of these structures in the context of some promising therapeutic or diagnostic applications being investigated today. We will conclude by providing our perspective on what we believe are promising horizons in the field of optical hybrid nanostructures.

# 1 Introduction

Understanding how a nanostructure absorbs, scatters, and/or reflects incident light provides critical information enabling the design of systems containing optical nanostructures for a wide variety of applications. Calculating these quantities depends upon the ability to solve Maxwell's equations when light is incident upon nanostructures<sup>1</sup>, where Maxwell's equations,

in the limit of non-magnetic materials of interest here, can be written in terms of space and time as

$$\epsilon_0 \frac{\partial \mathbf{E}(\mathbf{x}, t)}{\partial t} = \nabla \times \mathbf{H}(\mathbf{x}, t) - \frac{\partial \mathbf{P}(\mathbf{x}, t)}{\partial t} \quad (1)$$

$$\mu_0 \frac{\partial \mathbf{H}(\mathbf{x}, t)}{\partial t} = -\nabla \times \mathbf{E}(\mathbf{x}, t) \quad (2)$$

$$\nabla \cdot \mathbf{D} = \rho \quad (3)$$

$$\nabla \cdot \mathbf{B} = 0 \quad (4)$$

Here,  $\mathbf{E}$  and  $\mathbf{H}$  are the electric and the magnetic fields, and  $\mathbf{P}$  is the polarization density field, the vector  $\mathbf{x}$  represents the spatial variables of the system, and  $t$  denotes the time variable. The electric displacement field,  $\mathbf{D}$ , and the magnetic induction,  $\mathbf{B}$ , are related to the electric and magnetic fields by the constitutive relationships,

$$\mathbf{D} = \epsilon_0 \epsilon \mathbf{E} \quad (5)$$

$$\mathbf{B} = \mu_0 \mu \mathbf{H}, \quad (6)$$

where the dependence of the fields on space and time is implied. We will confine our attention here to non-magnetic materials, where the permeability  $\mu = 1$ . However, the permittivity of the material,  $\epsilon$ , may take on complex values that depend on frequency for many materials of interest. The frequency dependence of the permittivity may be considered naturally by considering the field equations in the frequency domain. Introducing complex frequency domain functions,  $\hat{\mathbf{E}}(\mathbf{x}, \omega)$ , such that  $\mathbf{E}(\mathbf{x}, t) = \hat{\mathbf{E}}(\mathbf{x}, \omega) \exp(-i\omega t)$ , etc., for each of the fields, the above time-domain equations yield the vector wave equation

$$\nabla \times \nabla \times \hat{\mathbf{E}}(\mathbf{x}, \omega) = \left(\frac{\omega}{c}\right)^2 \epsilon(\mathbf{x}, \omega) \hat{\mathbf{E}}(\mathbf{x}, \omega) \quad , \quad (7)$$

where  $\mu_0\epsilon_0 = 1/c^2$  has been used, the polarization has been assumed to vary linearly with the electric field,  $\hat{\mathbf{P}}(\mathbf{x},\omega) = \chi\hat{\mathbf{E}}(\mathbf{x},\omega)$ , and  $\epsilon(\mathbf{x},\omega) \equiv 1 + \chi(\mathbf{x},\omega)$ . As indicated before, the permittivity  $\epsilon$  may be (and often is) frequency dependent and complex. Time-dependent approaches to solving Maxwell's equations typically start from Eqs. (1) and (2), whereas Eq. (3) or variations thereof, supplemented by appropriate boundary conditions, generally represent the starting point of frequency-domain solution methods. If the system is invariant along one axis, then Eq. (3) may be replaced with a scalar wave-equation, frequently called the Helmholtz equation. This indeed applies to spherical particles represented in spherical polar coordinates, and it is the solution of the scalar wave equation underlies Mie theory<sup>2</sup>.

Inspection of Maxwell's equations reveals that the properties of its solutions depend directly upon the material properties of the objects interacting with the electromagnetic (EM) field, through the constitutive relations, and the geometry of the objects, through the boundary conditions these geometries impose upon the EM fields. The significance of this simple observation is that we can view the geometry and material properties as the fundamental ingredients for designing the optical properties of nanostructures. Indeed, one of the beautiful features of hybrid nanostructures is that heterogeneous domains can lead to surprising and non-trivial modifications both of the material properties of the constituent objects, and of the boundary conditions imposed by the structures on optical fields. One example of the former can be seen in very small bimetallic nanoparticles where interactions between the two metallic domains lead to a striking departure of the permittivity from bulk behavior. Sun, Foley, *et al.*<sup>3</sup> have shown that such bimetallic particles support emergent optical phenomena known as charge transfer plasmons. Related phenomena have been observed in nearly-touching nanoparticle dimers. In these systems, electron tunneling across the small interparticle gap dramatically changes the resonant properties of the structure, and the resonant behavior can be phenomenologically modeled as two particles bridged by a medium with an effective permittivity that can be related to the tunneling current<sup>4-8</sup>; though we note that rigorous treatment of this phenomena lies beyond the scope of classical

electrodynamics. An example of emergent behavior that arises purely from the boundary conditions on the electromagnetic waves can be seen when two different metal films are laterally interfaced. The presence of this interface presents an unusual boundary condition on surface waves propagating across it such that the waves refracted across this interface will take on the form of *inhomogeneous surface waves*, waves that have distinct propagation and decay directions<sup>9</sup>.

A wide variety of theoretical methodologies exist for solving Maxwell's equations either in the time-domain (see for example Refs. 10,11), or in the frequency domain (see for example Refs. 2,12–14). Time-dependent approaches of solving Maxwell's equations typically start from the first-order time-dependent electric and magnetic field equations, whereas frequency domain methods usually take the second-order frequency-dependent wave equation, supplemented by appropriate boundary conditions, as their starting point. In a few cases, Maxwell's equations can be solved analytically; indeed, under some often reasonable approximations, the analytical solutions can even be written simply, which greatly aids intuition about the behavior of a nanostructure. Two important analytical examples which will be considered include the interaction of light with spherical nanostructures solvable by Mie theory, and the interaction of light with planar nanostructures, solvable by the Transfer Matrix method. These simple structures both have their own interesting optical interactions (localized surface plasmons on metal nanospheres, surface plasmon polaritons on metal nanofilms, to name two) and are important elements for constructing more elaborate hybrid nanostructures. Furthermore, the simple act of bringing two similarly-sized nanospheres into close proximity or into contact can dramatically change their optical response, where examples include again nearly-touching dimers (see, for example, Refs. 4–8), touching dimers (see, for example, Refs. 3,15), and core-shell nanoparticles (see, for example, Refs. 16–18). Similarly, arranging thin films so that they are interfaced either vertically (multi-layer stacks, see for example Refs.<sup>19–21</sup>) or horizontally (similar to tiles, see for example Refs. 9,22,23) can also lead to dramatic changes in their optical response. In this chapter, we will consider in

detail several examples of the dramatic changes in optical response that occurs when simple nanostructures are brought together to form nanohybrids.

In the general case of hybrid nanostructures that do not have a high degree of symmetry that simplifies the solution of Maxwell's equations, numerical techniques must be employed for investigating their detailed optical properties. In this chapter, we will briefly discuss the finite-difference time-domain (FDTD) method and the discrete dipole approximation (DDA); the former solves Maxwell's equations in the time-domain, while the latter solves them in the frequency-domain. The finite element method, or FEM, is a frequency-domain approach capable of describing a great variety of problems<sup>14</sup>. The vectorial nature of Maxwell's equations make implementations of FEM significantly more sophisticated than DDA.

## 2 Theoretical Nanophotonics

The main thrust of nanophotonics research is to understand and control optical energy and information flow at nanoscale dimensions. The fundamental ways in which matter interacts with light changes as one or more of the features of that matter approach the nanoscale. Indeed, nanostructured matter can have a profound impact on light, having the potential to confine it well beyond the diffraction limit, slow it down to speed much slower than the speed of light in a vacuum, and impart it with much more momentum than it would carry while propagating freely<sup>24</sup>. The variety of tricks one can play with light using nanostructures seems to be similarly diverse as the types of nanostructures and nanostructure hybrids that can be imagined and constructed. A significant goal of this chapter is to highlight a small selection of this diversity, both from the authors' own work and from some recent contributions from others in the field. We will first begin by outlining the theoretical framework for understanding how light interacts with nanostructures. We will explicitly consider two particularly simple limits of nanostructures: spherical nanoparticles and planar nanostructures (nanofilms). For the former, all three of its spatial dimensions are

on the nanoscale; for the latter, only one of its spatial dimensions is on the nanoscale. For the sake of this chapter, we will refer to both of these types of structures as nanoelements since a multitude of more sophisticated hybrid structures can be constructed using them. Of course, one could identify a nanowire as yet another class of nanoelement, where two of its spatial dimensions are on the nanoscale. While there are many interesting properties of nanowires as well, we will not discuss them in detail in this chapter. In this section, we will outline several theoretical methodologies that can be used to calculate, analyze, and design the optical properties of simple and hybrid nanostructures. We will begin with two analytical approaches which can be used for spherical nanoelements (Mie theory) and planar nanoelements (Transfer Matrix Theory). We will then describe two popular numerical approaches that can be used for more general nanostructures, namely the Finite-Difference Time-Domain method and the Discrete Dipole Approximation. In principle, these numerical methods are capable of exactly calculating the linear optical properties arising from the classical electrodynamics of any nanoelement or hybrid nanostructure; the difficulty lies in the amount of computational effort that must be expended to do so.

## 2.1 Mie theory for spherical nanostructures

We consider spherical nanoparticles as the first example of a simple nanoelement; all three spatial dimensions of such a particle has nanoscale dimensions. These are perhaps the simplest nanostructures one can imagine, and indeed they have the longest history in terms of their use as a nanotechnology; the use of noble metal nanoparticles to provide color in stained glass was used in antiquity (for example, in the famous Lycurgus cup). The theoretical framework for understanding the optical properties of spherical nanoparticles also has a fairly long history compared to modern nanoscience, with the rigorous treatment developed by Mie in 1908. Used judiciously, Mie theory can be leveraged to understand a wide variety of optical phenomena that arise from spherical nanostructures, and to design these structures for various applications, as we will discuss.

Mie theory provides an analytical solution for Maxwell's equations when light is incident upon a spherical particle. A key idea behind Mie theory is to write the field components, including the scattered and internal (inside the particle) components, as an expansion in a spherical multipole basis, allowing Eq. (7) to be replaced with a scalar wave equation<sup>2,25</sup>. Using Maxwell's equations as conditions on the fields in this expansion leads to closed-form expressions for the expansion coefficients. Quantities like the absorption, scattering, and extinction cross section of the particle can be easily computed in terms of these coefficients<sup>2</sup>,

$$C_{scat} = \frac{2\pi}{k^2} \sum_{n=1}^{\infty} (2n+1) (|a_n|^2 + |b_n|^2) \quad (8)$$

$$C_{ext} = \frac{2\pi}{k^2} \sum_{n=1}^{\infty} (2n+1) \operatorname{Re}(a_n + b_n) \quad (9)$$

$$C_{abs} = C_{ext} - C_{scat}, \quad (10)$$

where  $k$  denotes the wavevector of incident light, and  $a_n$  and  $b_n$  are the expansion coefficients, which depend on particle size, particle composition, and frequency of the incident light. The computational effort scales linearly with the number of terms in the expansion, which can be reasonably truncated. An excellent discussion of Mie theory, as well as practical source code, can be found in Ref. 2.

For a particle with radius  $r$  very small compared to the incident wavelength of light, this expansion can usually be truncated after the dipolar term, which yields particularly simple forms for the absorption and scattering cross sections<sup>2</sup>,

$$C_{abs} = 4\pi\sqrt{\epsilon_m}\frac{\omega}{c}r^3 \operatorname{Im}\left(\frac{\epsilon_p(\omega) - \epsilon_m}{\epsilon_p(\omega) + 2\epsilon_m}\right) \quad (11)$$

$$C_{scat} = \frac{8\pi\epsilon_m^2\omega^4r^6}{3c^4} \left|\frac{\epsilon_p(\omega) - \epsilon_m}{\epsilon_p(\omega) + 2\epsilon_m}\right|^2. \quad (12)$$



Here  $\epsilon_p(\omega)$  denotes the permittivity of the particle (which we have allowed to be complex and to depend on the angular frequency,  $\omega$ ), while  $\epsilon_m$  denotes the permittivity of the surrounding medium (which we assume to be static and real). This expression predicts particularly large scattering and absorption cross sections at frequencies where  $\text{Re}(\epsilon_p(\omega)) = -2\epsilon_m$ . This equality is satisfied by many metallic nanostructures at visible frequencies, and is the condition for a localized surface plasmon resonance (LSPR), collective electronic oscillations that concentrate optical energy near the surface of nanostructure. LSPR in metal nanostructures is one means of confining optical energy and information down to nanoscale dimensions, well beyond the optical diffraction limit<sup>24</sup>.

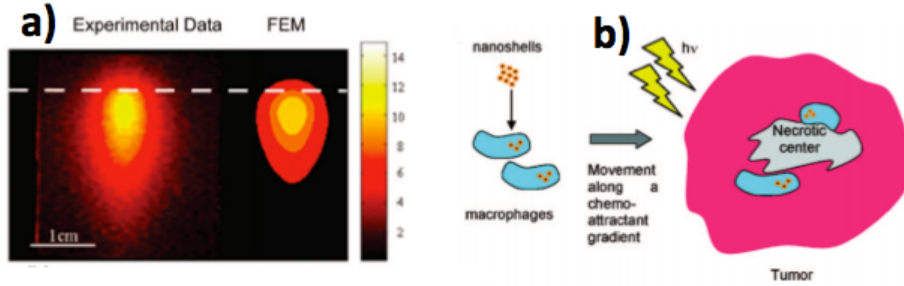


Figure 1: **a)** Experimental and theoretical (from finite element method (FEM) simulations) of near-field heating from SPR of core-shell nanoparticles in tissue-like medium. **b)** Schematic of photothermal therapy strategy that targets delivery of nanoshells for photothermal therapy to hypoxic tumor cells. Figures reproduced with permission from Ref. 26.

Spherical nanostructures are natural building blocks for more intricate hybrid nanostructures. That said, spherical nanostructures themselves can be used for a variety of therapeutic and diagnostic applications that leverages their optical properties. In these cases, the simplicity of Mie theory is certainly a boon in terms of the ability to formulate simple and robust design methodologies. One prominent example is that of photothermal cancer therapy mediated by spherical core-shell nanoparticles (see Figure 1 for an illustration of the concept of photothermal therapy, reviews on this topic can be found in Refs. 26,27). In this application, the resonant properties of dielectric-core metal-shell nanoparticles are tuned so that they support LSPR at near-infrared frequencies, which ultimately allows the localiza-

tion of thermal energy to the nanoscale volume of the nanostructure. These structures can be selectively introduced into tumor cells, and because tissue is maximally transmissive at near-infrared frequencies, it is relatively easy to illuminate the structures localized to the tumor cite. Sufficient heat is generated from the plasmon relaxation to induce cell death to the tumor without damaging the surrounding tissue. The resonant properties of these structures can be rigorously treated with Mie theory, and the small-particle limit of Mie theory is particularly illustrative of the key features of these structures that make them sufficiently tunable for this application. The absorption cross section of these structures, just like in the simple spherical case, is proportional to the imaginary part of the polarizability  $\alpha$ . The polarizability of a core-shell structure is given by<sup>28</sup>

$$\alpha = \frac{\epsilon_2 \epsilon_a - \epsilon_2 \epsilon_b}{\epsilon_2 \epsilon_a + 2\epsilon_3 \epsilon_b}, \quad (13)$$

where

$$\epsilon_a = \epsilon_1(3 - P) + 2\epsilon_2 P, \quad (14)$$

$$\epsilon_b = \epsilon_1 P + \epsilon_2(3 - P), \quad (15)$$

$$P = 1 - \left(\frac{r_1}{r_2}\right)^3, \quad (16)$$

and  $\epsilon_1$  is the permittivity of the core layer,  $\epsilon_2$  is the permittivity of the shell layer, and  $\epsilon_3$  is the permittivity of the medium surrounding the core-shell particle. When one or both of the core-shell materials is metallic, the core-shell structure can support a LSPR when  $\text{Re}(\epsilon_2 \epsilon_a = -2\epsilon_3 \epsilon_b)$ . The dependence on this term on the ratio of the core and shell radii enables considerable tunability of the resonance condition, which has made them particularly suitable for photothermal applications as discussed. Figure 2 illustrates the high tunability of glass core/gold shell nanostructures.

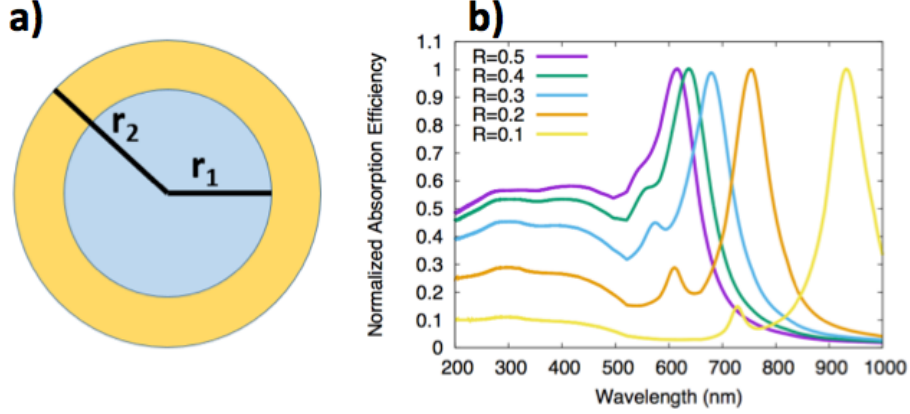


Figure 2: **a)** Schematic of glass-core gold-shell nanoparticles. **b)** Absorption spectrum of glass-core gold-shell nanoparticles with total radius  $r_2$  fixed at 50 nm with various ratios of  $r_2$  to  $r_1$ . The quantity  $R$  is related to the particle geometry by  $R = r_2/r_1 - 1$ .

## 2.2 Transfer Matrix Methods for Planar Structures

Planar structures form another nanoelement that can be used to construct interesting hybrids. The simplest planar structure of interest as a nanostructure is one whose axial dimension has nanoscale thickness, and is bounded on either side by semi-infinite media. If the nanofilm is metallic, like the gold nanofilm illustrated in Figure 3, then it can support surface waves known as surface plasmon polaritons (SPPs, see, for example, Refs. 24,25,29). If the nanofilm is a polar material, it can support surface waves known as surface phonon polaritons (SPhPs, see, for example, Refs. 30,31). These optical phenomena allow the nanoscale confinement of propagating optical energy and information at visible and near-IR frequencies for SPPs and wavelengths spanning mid-IR and terahertz frequencies for SPhPs.

For general  $L$ -layer planar structures layered along the  $z$ -axis (and isotropic along the  $x$ - and  $y$ -axes), the optical fields can be written in a piece-wise fashion as plane waves, and closed-form expressions for the wavevectors and amplitudes of the fields in each layer can be determined from considerations of Maxwell's equations and appropriate boundary conditions. The boundary conditions can be expressed conveniently as matrix equations, and the amplitudes can be computed by straightforward matrix multiplication, which forms the basis of what is called the Transfer Matrix Method<sup>12</sup>. We will present a Transfer Matrix

formalism that is capable of exactly computing many important linear optical quantities involving planar structures including reflectance, absorbance, transmittance, and the field distributions in each layer so long as each layer is isotropic in 2 dimensions.

The general Transfer Matrix equations for an  $L$ -layer system can be written as

$$\begin{pmatrix} E_1^+ \\ E_1^- \end{pmatrix} = \begin{pmatrix} M_{1,1} & M_{1,2} \\ M_{2,1} & M_{2,2} \end{pmatrix} \begin{pmatrix} E_L^+ \\ E_L^- \end{pmatrix}, \quad (17)$$

where the elements  $M_{i,j}$  depend on the material properties (the refractive index,  $n$ ) and geometry of each layer, as well as the frequency and polarization of incident light. This formalism assumes that layer 1 and layer  $L$  are semi-infinite materials with real refractive indices; however, all intermediate layers have finite thickness and may consist of materials with complex refractive indices. The 2x2  $\mathbf{M}$  matrix above can be computed from the following matrix product,

$$\begin{pmatrix} M_{1,1} & M_{1,2} \\ M_{2,1} & M_{2,2} \end{pmatrix} = \mathbf{D}_1^{-1} \left( \prod_{l=2}^{L-1} \mathbf{D}_l \mathbf{P}_l \mathbf{D}_l^{-1} \right) \mathbf{D}_L. \quad (18)$$

The  $\mathbf{P}$  matrix is defined for each finite-thickness layer as

$$\mathbf{P}_l = \begin{pmatrix} \exp(i \phi_l) & 0 \\ 0 & \exp(-i \phi_l) \end{pmatrix}, \quad (19)$$

where  $\phi_l = k_{z,l} d_l$  where  $d_l$  is the thickness of the  $l^{th}$  layer of the structure,

$$k_{z,l} = \sqrt{\left(n_l \frac{\omega}{c}\right)^2 - \left(n_1 \sin(\theta_1) \frac{\omega}{c}\right)^2} \quad (20)$$

$\theta_1$  is angle of incidence of light of frequency  $\omega$  upon the structure, and  $n_l$  is the refractive index of the  $l^{th}$  layer. If the incident light is s-polarized, then the  $\mathbf{D}$  matrix for layer  $l$  has

the form

$$\mathbf{D}_l = \begin{pmatrix} 1 & 1 \\ n_l \cos(\theta_l) & -n_l \cos(\theta_l) \end{pmatrix}, \quad (21)$$

while the  $\mathbf{D}$  matrix has the form

$$\mathbf{D}_l = \begin{pmatrix} \cos(\theta_l) & \cos(\theta_l) \\ n_l & -n_l \end{pmatrix}, \quad (22)$$

if the incident light is p-polarized. Again,  $n_l$  is the refractive index of the  $l^{th}$  layer, and  $\theta_l$  is the angle of refraction in the  $l^{th}$  layer, which is governed by Snell's law<sup>12</sup>.

We interpret  $E_1^+$  and  $E_1^-$  as incoming and outgoing wave amplitudes on the incident side, respectively; similarly,  $E_L^-$  and  $E_L^+$  are incoming and outgoing wave amplitudes, respectively, on the terminal side of the structure. With the access to the field amplitudes and wavevectors, a number of useful quantities may be computed. For example, the Fresnel reflection and transmission amplitudes may be computed as  $r = E_1^-/E_1^+$ . If we set the incoming field amplitude to 1 on the incident side, then clearly the reflection amplitude is equal to the amplitude of the outgoing wave on the incident side:  $r = E_1^-$ . Furthermore, we may specify that the incoming wave amplitude on the terminal side is equal to zero, which physically corresponds to only having light incident upon layer 1. In this case, the only fields on the terminal side are outgoing waves that correspond to light transmitted through the structure, and the transmission amplitude is equal to the this outgoing wave amplitude:  $t = E_L^+$ . These conditions lead to the specific form of the TMM equations given by

$$\begin{pmatrix} 1 \\ r \end{pmatrix} = \begin{pmatrix} M_{1,1} & M_{1,2} \\ M_{2,1} & M_{2,2} \end{pmatrix} \begin{pmatrix} t \\ 0 \end{pmatrix}. \quad (23)$$

These equations lead directly to

$$1 = M_{1,1} t$$

$$r = M_{2,1} t,$$

which allow the calculation of the reflection and transmission amplitudes simply in terms of TMM matrix elements,

$$t = \frac{1}{M_{1,1}}$$

$$r = \frac{M_{2,1}}{M_{1,1}}.$$

The reflection can then be calculated as  $R = |r|^2$ , the transmission as  $T = |t|^2 n_L \cos(\theta_L) / (n_1 \cos(\theta_1))$ , where  $n_i$  and  $\theta_i$  denote the refractive index of the material of layer  $i$  and the incident/refraction angle in layer  $i$ , respectively. The absorption can simply be computed as  $A = 1 - T - R$ . The computational effort of the Transfer Matrix Method is minimal as it primarily involves the computation of the matrix elements  $M_{i,j}$ , which can be accomplished in a number of arithmetic operations that scales linearly with the number of layers in the structure.

The Transfer Matrix Equations can also be used to compute the dispersion for resonant modes in multi-layer structures. Two resonant modes of particular interest for multi-layer structures with one or more metallic layers include surface plasmon polariton (SPP) modes<sup>24,25,29,32–34</sup>, and perfectly absorbing (PA) modes<sup>34–37</sup>; the former occurs when  $R \rightarrow \infty$  and  $T = 0$ , while the latter occurs when  $R \rightarrow 0$  and  $T = 0$ . SPPs involve collective electronic oscillations coupled to a propagating electromagnetic wave, and they allow light to be guided along the 2-dimensional interface between a metal and a dielectric layer. Perfectly absorbing modes can allow perfect absorption of incident light, and perfect thermal emission of light, by thin absorbing layers. Unlike SPPs, PA modes are non-propagating<sup>34</sup>.

Both of these resonant phenomena (SPPs and PA modes) can be excited by an experimen-

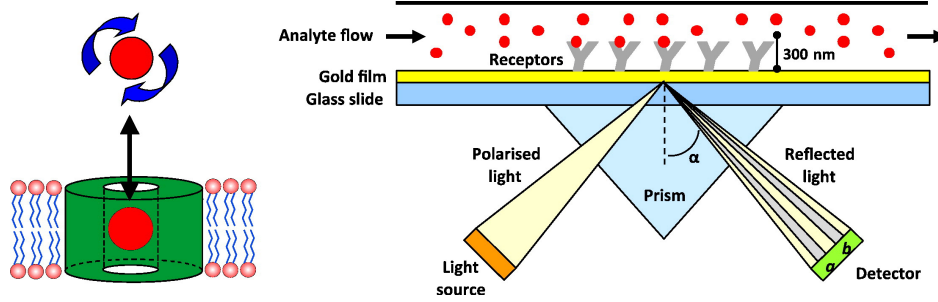


Figure 3: Schematic of system for spectroscopy of protein-ligand binding using that utilizes the resonant properties of metal nanofilms. Reproduced with permission from Ref. 38.

tal technique known as Kretschmann-Raether (K-R) excitation<sup>29</sup>. A simple implementation of K-R excitation could involve a thin ( 50 nm) noble metal film with a thick glass substrate and air above the metal film. K-R excitation in this example would involve light of a given frequency incident from the glass side. The in-plane momentum  $k_x$  of the incident light is given simply by

$$k_x = \frac{\omega}{c} n_{glass} \sin(\theta_i) \quad (24)$$

where  $n_{glass}$  is the refractive index of the glass substrate and  $\theta_i$  is the angle of incidence through the glass. Because both the SPP and PA resonances have well defined in-plane momentum for a frequency  $\omega$  that exceeds that of a photon in free space ( $\omega/c$ ), the incident light from the glass side layer can be perfectly matched to the momentum of the resonant mode, which allows optimal coupling into the resonance. A particular feature of the perfectly absorbing resonance is that the reflection reaches a minimum when the in-plane momentum of the incident light matches the momentum of the perfectly absorbing mode. The precise magnitude of the momentum can be found for a given frequency  $\omega$  using the transfer matrix method by solving for:

$$M_{2,1}(\omega, \beta, \alpha) = 0, \quad (25)$$

where  $\beta$  denotes the magnitude of the real component of the wavevector associated with the resonant mode, and  $\alpha$  denotes the magnitude of the imaginary component of the wavevector associated with the resonant mode. The quantity  $\beta$  can be mapped directly to the resonance

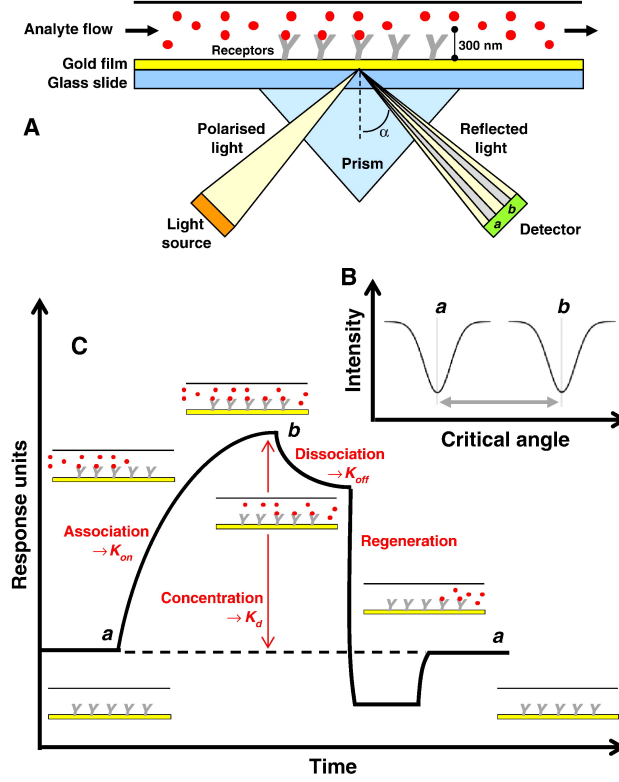


Figure 4: Illustration of the use of the resonant properties of a gold nanofilm for measuring thermodynamic quantities like the Gibbs free energy, enthalpy, and entropy of binding. Reproduced with permission from Ref. 38.

angle satisfying Eq. (24), that is, resonant coupling into the PA mode occurs when  $k_x = \beta$ . Under these conditions, the reflection is a minimum. The precise value of  $\beta$  is known to be very sensitive to the environment at the metal surface. In particular, small changes in the refractive index of the superstrate layer can lead to measurable changes in the resonant angle. This observation has been leveraged to design systems that probe the thermodynamics and kinetics of a variety of biochemically relevant processes, like ligand binding with membrane proteins, illustrated in Figure 3 and 4.<sup>38</sup> In this case, membrane proteins are immobilized to the superstrate side of the gold film, and the superstrate side is equipped with a flow cell that can introduce analyte molecules in solution (see Figure 3). Binding of analyte molecules to the membrane proteins monotonically increases the refractive index of the superstrate layer, which leads to a commensurate increase in the momentum of the PA mode and increase in the resonant angle required to couple optimally into the PA mode. Hence, the change in the



angle of the reflectance minimum can be precisely mapped to a change in the concentration of bound protein-analyte pairs, which allows measurement of the binding equilibrium constant and the Gibbs free energy of binding. Running this experiment at several temperatures allows the calculation of the enthalpy and entropy of binding through the van't Hoff equation. Finally, monitoring the time-dependence of binding allows the measurement of the binding kinetics. Consequently, this technique is quite promising for applications like drug discovery that rely on careful analysis of protein-ligand binding<sup>38</sup>. Such experiments are illustrated schematically in Figure 4.

### **2.3 The Finite-difference time-domain method**

For the optical behavior of more general structures, numerical approaches are often required to solve Maxwell's equations. Perhaps the most conceptually simple approach is known as the finite-difference time-domain (FDTD) method. Here the time evolution of the fields is computed using Maxwell's equations (specifically, the curl equations, Eq. (1) and (2)) where the spatial and temporal variables are discretized on a rectangular grid, and centered finite-differences are used for the derivatives in terms of these variables<sup>10</sup>. The electric and magnetic fields are spatially staggered on the computational grid, which automatically enforces Gauss' laws (Eq. (3) and (4)), thus the algorithm only explicitly treats the curl equations (Eq. (1) and (2))<sup>10</sup>. Quantities such as absorption, scattering, reflection, and transmission can be defined in terms of fluxes of electromagnetic fields. Electric field distributions and other quantities may be obtained in the frequency domain by the appropriate Fourier transform of the time-domain fields. The permittivity of metals and semiconductors can have strong frequency dependence across the UV/Vis/IR spectrum, and this frequency dependence requires some consideration for time-domain simulations like FDTD. Material dispersion leads to time-dependence of the material susceptibility and causes the polarization density to depend on field values at all previous times. This is commonly handled by fitting the permittivity to an analytical function of frequency, commonly a sum of Drude and

Lorentz oscillator functions, so that the convolution can be easily computed. A practical drawback is that it can be difficult to obtain a good fit for these functions across a broad spectrum for highly-dispersive materials.

The computational effort of FDTD scales with the 4<sup>th</sup> power of the computational domain for simulations with 3 spatial and 1 temporal dimension. The spatial grids are generally discretized with grid spacing  $d$ , where  $d$  is a value less than the structural features of the material being studied and less than the sub-wavelength electromagnetic field variations resulting from the optical response materials being studied. The time-step is usually defined relative to the spatial grid size by the Courant factor<sup>10</sup>. This tends to make simulations of structures with several disparate length-scales challenging, as a small grid size is required for the smallest feature, while many grid elements are required to span the physical structure. However, FDTD implementations can utilize multi-resolution grids to reduce the computational effort in these cases. Furthermore, FDTD simulations can exploit symmetry, periodicity, and can be massively parallelized, all of which has enabled their application to a variety of complex systems.

Many codes like Lumerical<sup>39</sup>, a commercial-grade FDTD simulator, and MEEP<sup>11</sup>, an open-source FDTD code, have scripting capabilities and other built-in tools to perform sweeps and optimizations over system variables, including material constants and geometric parameters. These sorts of scripting interfaces also allow the user to extract a variety of indirect or derived quantities; for example, the net energy flux between isolated structures may be desired to optimize near-field radiative heat transfer<sup>30</sup>, which may be of interest for designing structures for photothermal therapy as previously discussed. Surfaces with periodic patterns, generally termed 2D photonic crystals, are also readily modeled using FDTD approaches due to their high degree of symmetry. These types of structures may be designed to support PA and SPP-like modes, and can therefore be put to use for similar experiments as were described for probing the thermodynamics of binding. This prospect is particularly appealing because the optical properties of these structures that govern the

resonant behavior can be tuned via geometric parameters like the periodicity, which can enhance the sensitivity and flexibility of systems based on these structures.

## 2.4 The Discrete Dipole Approximation

Several computational methodologies for solving Maxwell's equations in the frequency domain are also available, and here we focus on the Discrete Dipole Approximation (DDA), which is particularly useful for problems involving scattering and light absorption from particles. The idea behind DDA is to represent scattering structures by an array of  $N$  dipoles. In DDA, each dipole has a polarization given by  $\mathbf{P}_j = \alpha_j \mathbf{E}_j$ , where  $\mathbf{E}_j$  is the electric field at the discrete point occupied by dipole  $j$ , and  $\alpha_j$  is the polarizability of dipole  $j$ , which is determined from the permittivity of the material being modeled<sup>13</sup>. The electric field at the position  $j$  of a given dipole is expanded as

$$\mathbf{E}_j = \mathbf{E}_{inc,j} - \sum_{k \neq j}^N \mathbf{A}_{j,k} \mathbf{P}_k. \quad (26)$$

The incident field ( $\mathbf{E}_{inc,j}$ ) has the form of a monochromatic plane wave, and the product  $-\mathbf{A}_{j,k} \mathbf{P}_k$  gives the electric field at point  $j$  due to the polarization at point  $k$ ; hence, the matrix  $\mathbf{A}$  carries information about the geometry and polarizability of the dipoles. The polarization is found by solving the system of linear equations given by  $\sum_{k=1}^N \mathbf{A}_{j,k} \mathbf{P}_k = \mathbf{E}_{inc,j}$  where the diagonal elements of  $\mathbf{A}$  have the known form  $\mathbf{A}_{jj} = \alpha_j^{-1}$ . Iterative methods are used to solve this equation, leading to overall quadratic scaling of the computational effort with the number of dipoles<sup>13</sup>. Extinction and absorption cross sections may be written in terms of  $\mathbf{P}$ <sup>13</sup>:

$$C_{ext} = \frac{4\pi k}{|\mathbf{E}_0|^2} \sum_{j=1}^N \text{Im}(\mathbf{E}_{inc,j}^* \cdot \mathbf{P}_j) \quad (27)$$

$$C_{abs} = \frac{4\pi k}{|\mathbf{E}_0|^2} \sum_{j=1}^N \left( \text{Im}(\mathbf{P}_j \cdot (\alpha_j^{-1})^* \mathbf{P}_j) - \frac{2}{3} k^3 |\mathbf{P}_j|^2 \right). \quad (28)$$

In general, high resolution can be obtained for small structures with a relatively small number of dipoles, and so DDA can be extremely efficient for modeling the optical properties of nanoparticles. DDAs formulation in the frequency domain also makes it more convenient than FDTD for modeling materials whose permittivity depends strongly on frequency since the permittivity as a function of frequency can be fed directly into the simulation. While scattering is solved for one frequency at a time, DDA can be run in parallel over the desired frequency range. One considerable drawback is that convergence of the DDA method, both in terms of the number of iterations for solving the linear equations and in terms of the accuracy of the polarization with respect to the number of dipoles, can be quite challenging for materials with large real or imaginary components of refractive index<sup>40</sup>. Silver is a classic material for which DDA modeling presents a particular challenge at visible frequencies. Interesting recent developments in DDA of relevance to applications like photothermal therapy include variations of DDA that are capable of describing particle-surface interactions<sup>41</sup> and near-field radiative heat transfer<sup>42</sup>.

### 3 Hybrid Nanostructures

With the theoretical underpinnings, and associated computational methodologies, for analyzing the optical properties of nanostructures in place, we now discuss some of the phenomenology that makes hybrid nanostructures promising for a variety of potentially transformative health applications.

#### 3.1 Emergent electrodynamics phenomena: Inhomogeneous Surface Plasmon Polaritons

An example of emergent electrodynamics behavior can be seen when surface plasmon polaritons refract at metal-metal interfaces, as shown in Figure 5 (a). Because SPPs are exponentially confined both above and below a surface, one can attempt to describe their

motion using classical optics ideas applied to the 2-D propagation plane. SPPs have been shown experimentally to exhibit refraction behavior when they propagate across an interface between two metal/dielectric interfaces with differing optical properties.<sup>22,23</sup> Negative refraction of SPP-dominated waveguide modes has also been achieved.<sup>43</sup> In general, the refracted waveform of an ISPP on the second metal surface is an inhomogeneous wave, which has been termed an inhomogeneous surface plasmon polariton (ISPP)<sup>9</sup> (see Figure 5 (b)). The characteristic feature of an ISPP is that its lines of constant phase and amplitude are nonparallel; that is, its propagation and decay directions are different. By contrast, ordinary SPPs are homogeneous waves in the 2-D plane and are attenuated exactly along their direction of propagation. Refraction can be exploited to introduce significant confinement in ISPPs without sacrificing propagation length. ISPPs propagating on the second metal surface also exhibit properties that depend on the angle of incidence and optical properties of SPPs on the first metal surface. For example, ISPPs on the second metal can exhibit different dispersion relations than ordinary SPPs on that same metal. These dispersion relations can actually exhibit features of the dispersion relations of ordinary SPPs on the first metal surface. We term this effect dispersion imprinting since, for example, the dispersion relation of an ISPP on an aluminum surface, arising from refraction of an SPP on a gold surface, can resemble the dispersion of ordinary SPPs on the gold surface. Importantly, dispersion imprinting can allow the extension of the SPP dispersion to frequencies higher than the ordinary back-bending frequency, for example, by the conversion of a radiative Brewster mode<sup>24</sup> into a bounded SPP mode. A more complete treatment of the theory of ISPPs is given in Ref. 9. Here we quote the main results. Portions of the following development of the theory of ISPPs is adapted from Ref. 9 as permitted by the ACS Journal Publishing Agreement.

Metal-metal interfaces, as illustrated in Figure 5, impose boundary conditions on the complex wavevectors of the incident and refracted waves. The incident wave is an ordinary

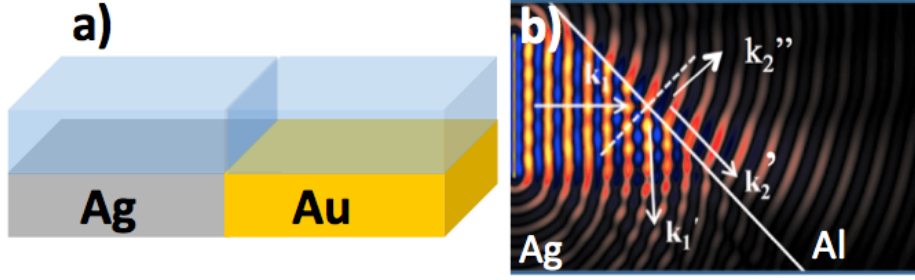


Figure 5: **(a)** Schematic of laterally interfaced metallic thin films, which are hybrid nanostructures that can support an emergent electrodynamics phenomenon known as inhomogeneous surface plasmon polaritons (ISPPs). **(b)** Finite-difference time-domain simulation of an experiment where an ISPP is excited on an aluminum surface by an ordinary SPP propagating on a silver surface. The ordinary SPP wavefront encounters the silver/aluminum interface at an angle. The continuity of the tangential components of the wavevectors of the incident SPP and the refracted ISPP are given by a complex generalization of Snell's law, which predicts that the real and imaginary components of the refracted ISPP wavevector will have different angles relative to the angle of incidence. This introduces lateral confinement to the ISPP waveform. In this figure, the real component of the ISPP wavevector is denoted  $\mathbf{k}_2'$  and the imaginary component of the ISPP wavevector is denoted  $\mathbf{k}_2''$ . Reproduced with permission from Ref. 9.

SPP, and we denote its wavevector simply as

$$\mathbf{k}_1 = \frac{\omega}{c} (\eta_1 + i\kappa_1) \hat{\mathbf{e}}, \quad (29)$$

where  $\hat{\mathbf{e}}$  is a unit vector pointing along the propagation and attenuation direction of the wave; this is to say that the incident SPP is a *homogeneous wave*. For a semi-infinite metal layer with permittivity  $\epsilon_{1,m}(\omega)$  with a semi-infinite dielectric superstrate with permittivity  $\epsilon_{1,D}$ , the magnitudes of the wavevector can be calculated simply as

$$\eta_1 + i\kappa_1 = \left( \frac{\epsilon_{1,m}(\omega)\epsilon_{1,D}}{\epsilon_{1,m}(\omega) + \epsilon_{1,D}} \right). \quad (30)$$

Of course, the Transfer Matrix Method can be used to find these magnitudes in general. The refracted wave is in general found to be an inhomogeneous wave, and we write the wavevector of it as

$$\mathbf{k}_2 = \frac{\omega}{c} \left( N_2 \hat{\mathbf{a}} + iK_2 \hat{\mathbf{b}} \right), \quad (31)$$

where  $\hat{\mathbf{a}}$  is a unit vector pointing along the propagation direction and  $\hat{\mathbf{b}}$  is a unit vector pointing along the attenuation direction of the wave; this is to say that the refracted SPP is an *inhomogeneous wave*. The tangential component of the real and imaginary parts of the wavevectors must be continuous across the metal-metal interface, which leads to the complex generalization of Snell's law:

$$\eta_1 \sin(\theta_1) = N_2 \sin(\theta_2) \quad (32)$$

$$\kappa_1 \sin(\theta_1) = K_2 \sin(\phi_2). \quad (33)$$

The wavevector magnitudes of the refracted ISPP must obey the following conditions:

$$N_2^2 - K_2^2 = \eta_2^2 - \kappa_2^2 \quad (34)$$

and

$$N_2 \cdot K_2 \cos(\theta_2 - \phi_2) = \eta_2 \cdot \kappa_2, \quad (35)$$

where  $\eta_2$  and  $\kappa_2$  are the ordinary SPP indices, which may be found as already described for  $\eta_1$  and  $\kappa_1$ . One can then arrive at an explicit expression for the *effective* ISPP index

$$N_2 = \frac{1}{\sqrt{2}} \sqrt{a + \sqrt{b}} \quad (36)$$

where

$$a = \alpha_1^2 + \beta_1^2 + \eta_2^2 - \kappa_2^2, \quad (37)$$

$$b = ((\kappa_2 - \beta_1)^2 + (\eta_2 - \alpha_1)^2) ((\kappa_2 + \beta_1)^2 + (\eta_2 + \alpha_1)^2), \quad (38)$$

$$\alpha = \eta_1 \sin(\theta_1), \quad (39)$$

and

$$\beta_1 = \kappa_1 \sin(\theta_1). \quad (40)$$

The key result here is that the effective indices of the refracted ISPPs are observed to depend not only upon the medium that they are propagating on (the metal 2/dielectric 2 interface), but also upon the incident angle of the ordinary SPP used to excite it, as well as the material that the incident ordinary SPP was propagating on. To see this, we can expand the expression for the real part of the effective ISPP index to leading order as

$$N_2^2 \approx \eta_2^2 + \kappa_1 \sin(\theta_1) - 2\eta_1 \sin(\theta_1). \quad (41)$$

This unexpected result highlights a new way in which the properties of surface waves may be controlled. Several other interesting consequences arise from the properties of ISPPs. Recalling the definition of inhomogeneous waves, we see that the propagation and decay directions of the ISPPs are unique, while these directions are the same for ordinary SPPs. Therefore, *propagation length* ( $L_P$ ), the measure of the distance that an SPP propagates before its field intensity decays to  $1/e$  of its initial value, must be redefined for ISPPs. What we require is knowledge of the *projection* of the imaginary part of the ISPP wavevector onto the real part of the ISPP wavevector. Therefore, the expression

$$L_P = \frac{1}{2k_0 K_2 \cos(\theta_2 - \phi_2)} \quad (42)$$

tells us how far the ISPP propagates along the propagation direction before its field intensity decays to  $1/e$  of its initial value. It is immediately apparent that there must be a decay component in the direction orthogonal to the propagation direction. This decay component gives rise to the unusual feature of lateral confinement of the ISPP. A quantity we termed the *confinement length* ( $L_C$ ) can be defined to measure the distance in the direction orthogonal



to travel at which point the ISPP field intensity decays to  $1/e$  of its initial value,

$$L_C = \frac{1}{2k_0 \sin(\theta_2 - \phi_2)}. \quad (43)$$

### 3.2 Advancing imaging beyond the diffraction limit with ISPPs

This last expression illustrates one of the remarkable features of ISPPs, which is the ability to introduce lateral confinement, in addition to axial confinement, of the ISPP field beyond the diffraction limit. If highly confined ISPP fields are used as the excitation source for a fluorescently labeled sample, the excitation profile would be expected to follow the intensity profile of the ISPP; that is, only fluorophores in the region of high-field intensity would have a high probability of being excited (see Figure 6 for an illustration of this concept). Limiting the excitation of fluorophores to sub-diffraction limited regions is one possible way to achieve super-resolution imaging<sup>44</sup>.

For ordinary SPPs, sub-wavelength confinement is only possible in the axial dimension (normal to the metal-dielectric interface). From the perspective of health applications, it is particularly tantalizing to think of applying the additional confinement capabilities of ISPPs to advance super-resolution microscopy techniques for imaging biological systems. Currently, total internal reflection microscopy (TIRFM) is a robust microscopy technique that relies on axial confinement of evanescent waves (generated through total internal reflection) to achieve super-resolution in the  $z$  axis of a sample<sup>44</sup>. That is, the intensity profile of the evanescent wave is subject to sub-diffraction control in the axial dimension, which results in sub-diffraction limit control of fluorescence excitation in the axial dimension. However, the lateral resolution of TIRFM remains diffraction limited. ISPPs present the ability to introduce this lateral resolution in a configuration which is quite similar to that already utilized by TIRFM, but with a heterogeneous metal nanofilm replacing the glass film ordinarily utilized to generate the evanescent waves by TIR.

Consideration of Eq. (43) reveals that the lateral confinement of the ISPP wave can

be tuned through a number of controllable parameters, including the materials comprising the metal thin films (metal 1 and metal 2), the permittivity of the dielectric superstrate materials, and the angle of incidence. Two parameters, the angle of incidence and the permittivity of superstrate 1, are particularly interesting because these could be changed on the fly to adjust lateral resolution during an imaging experiment. In principle, the degree of lateral confinement can be tuned as desired by changing the angle of incidence in the refraction plane according to Eq. (43), and the the angle of incidence in the refraction plane can be controlled using a polarization filter coupled to the microscope objective.

Super-resolution in all dimensions can be achieved using crossed ISPP evanescent waves and two-photon absorption fluorophores (see Fig. 6). Such a technique could have advantages over existing super-resolution techniques including STED and GSD because it doesn't rely on high photon fluxes that can lead to cell damage in living systems<sup>44</sup>.

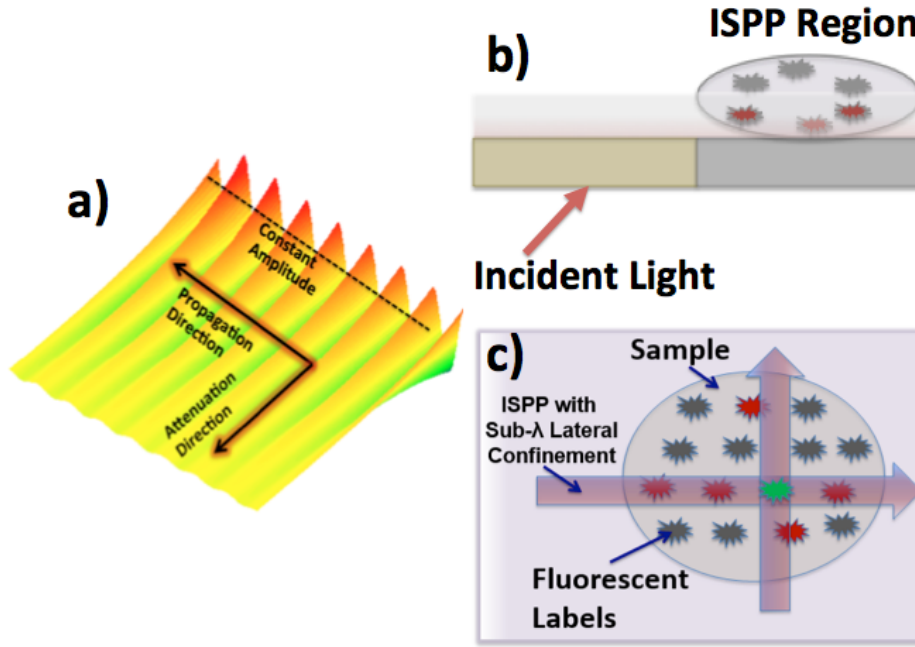


Figure 6: **a)** Illustration of the waveform of an ISPP with significant lateral confinement. **b)** Side-view schematic of evanescent mode imaging using ISPPs. **c)** Top-view schematic of evanescent mode imaging using ISPPs.

### 3.3 Emergent material-dependent optical response in hybrid nanostructures

Different emergent optical phenomena can be observed in hybrid nanostructures due to changes in the material properties that result from interactions between different domains in the hybrid structure. For example, it has been shown that in heterodimers with small ( $r \simeq 2$  nm) silver and gold spherical domains, quantum size effects, formation of the Au/Ag interfaces, and chemical interactions with surfactant molecules strongly influence the optical properties of the dimers and lead to the observation of unique surface plasmon resonances. In particular, unusual enhancement of the characteristic Au surface plasmon resonance and the emergence of a charge transfer plasmon across the Au/Ag domains has been observed<sup>3</sup>. These emergent phenomena lead to new and enhanced absorption spanning visible to near-infrared wavelengths. Here, we discuss this phenomenon, as well as a simple model for the permittivity that captures the changes in optical behavior due to chemical interactions and quantum size effects and can be used to calculate the absorption spectra of the interfaced heterodimers, resulting in good agreement with experimental measurements. The following discussion of this system and its phenomenology is adapted with permission from Ref. 3.

The SPRs of nanoparticles in the small particle limit can significantly deviate from SPRs of larger nanoparticles due to quantum size effects. For example, Scholl, Koh, and Dionne used monochromatic scanning transmission electron microscopy (STEM) and electron energy-loss spectroscopy (EELS) to study SPRs of individual ligand-free Ag nanoparticles with diameters ranging from 20 nm to less than 2 nm and identified a transition into a quantum regime characterized by a substantial blue-shift in the resonance position with decreasing particle size<sup>45</sup>. Sun and co-workers synthesized highly uniform colloidal Ag nanoparticles with varying diameters in the range of 220 nm. The SPR peak position of these colloidal Ag nanoparticles exhibited exceptional size dependence, that is, initially blue shifting as size decreased from 20 nm but then strongly red shifting with decreasing size from 12 nm down to 2 nm<sup>46</sup>. Theoretical modeling suggested that surfactant/Ag interactions lowered

the electron density of the surface Ag layer of the nanoparticles peaks. This effect has been termed a “quantum chemical” size effect. Size effects, of course, are not limited to isolated monomer systems. In nanoparticle dimer systems, the separation gap between the monomer units also provides an additional source of quantum size effects. Recent experimental and theoretical studies have demonstrated deviations from classical theories occurring for small gaps ( $< 1$  nm) and correlated these results with quantum tunneling<sup>4–8,47,48</sup>. The key point is that the electronic structure of small metal nanostructures can be strongly perturbed by the local environment. Since the optical properties are intrinsically related to the electronic structure via the material permittivity, we can view the construction of hybrid nanostructures as a means for tuning the optical properties through the permittivity itself. The ultimate realization of such a concept would be the ability to engineer the permittivity by the judicious construction of nanostructure hybrids. This prospect is appealing for a multitude of reasons. Firstly, it in principle allows the design of hybrid structures that display optical properties not found in pure materials. Second, there has recently been a resurgence in interest the use of plasmonic nanostructures for sources of energetic (or ‘hot’) electrons. Hot electron injection has been investigated as an operative mechanism for plasmon-mediated photocatalysis, and photocurrent generation in photovoltaic materials, to name a few. The energy distribution of hot electrons is itself intrinsically related to the electronic structure of the nanostructure. Hence, the ability to engineer the electronic structure of nanostructures through the construction of hybrid nanostructures offers new possibility in controlling the distribution of hot-electrons generated from plasmon decay. In the following paragraphs, we discuss in detail one example that illustrates this potential to enhance the optical response through modification of the permittivity resulting from the construction of hybrid nanostructures.

Sun, Foley, *et al.* reported the synthesis of high-quality interfaced Au/Ag heterodimers in the quantum size regime (diameters  $< 10$  nm) with the use of isotropic spherical Au nanoparticles as the starting materials. Each heterodimer consisted of a spherical Au nanoparticle

and a Ag nanoparticle epitaxially grown from the Au nanoparticle. The Au/Ag heterodimers were synthesized in high yield and the size of the Ag nanodomains were controlled by reaction time. Growth of the interfaced Ag nanodomains brought about several remarkable optical features, including an unexpected enhancement of gold’s SPR and the emergence of a broad, charge transfer plasmon (CTP). A CTP is characterized by charge oscillations between the separate domains in a nanostructure.<sup>7,8,17,48,49</sup> It was found that when the Ag domains are comparable or larger in size than the Au spheres, the CTP resonances contributed to broad-band absorption spanning visible to near-infrared wavelengths. The precise tunability of the structural features makes these particles especially suitable for performing comprehensive experimental and theoretical studies of the relationship between structure and the unique optical properties that arise from chemical interactions and quantum size effects in small hybrid nanostructures; such studies can provide valuable insight into how plasmonic materials can be engineered for catalytic, sensing, and other purposes in the small-particle limit.

The SPRs of the interfaced AuAg heterodimers were examined by measuring absorption spectra of the heterodimers dispersed in hexane. As shown in Figure 7, pure Au spherical nanoparticles exhibit a broad asymmetric absorption peak at 548 nm with a full width at half-maximum (fwhm) of 70 nm. Mie theory calculations for a spherical Au nanoparticle with a diameter of 5.9 nm immersed in hexane (dielectric constant 1.88) yields a peak more than twice as narrow (fwhm 30 nm) and centered on 525 nm (not shown) when the dielectric function of the bulk gold is used<sup>50</sup>. The broadness of the experimentally observed peak and its 20 nm red shift relative to the simple Mie theory result is ascribed to the surface damping associated with small size of the Au nanoparticles and chemical interactions with surfactant molecules<sup>46</sup>. Most interestingly, the peak intensity of the Au nanoparticles is significantly enhanced by about 50%, and the peak width is slightly narrowed upon formation of the AuAg interface at reaction time of 2 s (red curve, Figure 7). Because the Au nanoparticles are not changed during the deposition of the Ag domains, the changes of the absorption peak can be attributed to the formation of the Au/Ag interface. The absorption spectrum

of the interfaced AuAg heterodimers formed at 2 s does not show the characteristic Ag SPR band (expected to be near 410 nm), indicating that the formation of Au/Ag interface may damp the SPR in the Ag domains. Figure 7 further shows that as the Ag domains become larger (reaction times increase beyond 2 s), the absorption peak around the Au SPR position shifts to the red and a new absorption peak gradually develops around the characteristic Ag SPR position. A third SPR peak emerges near 600 nm at the reaction time of 90 s when the sizes of the Ag domains are similar to those of the Au nanoparticles. The absorption spectrum of the interfaced AuAg heterodimers, when the Au and Ag nanodomains are of comparable size, exhibit three well-defined peaks: (i) one at 410 nm close to the Ag SPR position, (ii) one at 540 nm close to the Au SPR position, (iii) one at longer wavelength ( $>600$  nm). In the remainder of the text, these absorption peaks are referred to as PK1, PK2, and PK3, respectively, for simplicity. As the Ag domains continue to grow, PK2 slightly blue shifts while PK3 significantly red shifts. Both the peaks gain intensity and eventually span overlapping spectral regions between 500 and 900 nm surface-to-volume ratio, we expect that quantum size effects and chemical interactions with surfactant molecules will contribute significantly to the observed SPR behavior. Indeed, classical electrodynamics calculations using the discrete dipole approximation (DDA)<sup>13,51</sup> and the bulk dielectric constant data of Johnson and Christy for Ag and Au<sup>50</sup> for the heterodimers immersed in hexane lead to absorption spectra that differ from the experimental results in several key aspects. Relative to the experimental results of Figure 7, the calculated peaks are both significantly narrower; PK1 at 180 s is calculated to have a fwhm of 25 nm compared to the experimentally measured fwhm of 50 nm and PK2 at 0 s is calculated to have a fwhm of 30 nm compared to the experimentally measured fwhm of 70 nm. Additionally, all three peaks are blue shifted by 20 – 30 nm in the calculated spectra when bulk properties are assumed. While small, the synthesized nanoparticles are still too large to allow for reliable, fully quantum mechanical calculations of their optical properties. Nonetheless we can account for quantum size effects and chemical interactions in a phenomenological manner by size-correcting the dielectric

constant of each of the metals in the heterodimer. DDA calculations, employing these size-corrected dielectric constants are then used to obtain absorption spectra and other quantities of interest. For each frequency or wavelength considered, the DDA calculations require specification of the dielectric constant at each point in space. For points in space that are within a given metal of the heterodimer, (i) the intraband contribution to the metals dielectric constant is modified to reflect damping of the conduction electrons<sup>46,52–56</sup> and (ii) for points within the outer 0.25 nm layer of the heterodimer, following Ref. 46, the intraband size correction also includes a reduction in conductivity in this outer layer owing to chemical interactions with the OAm surfactant. We assume that the heterodimer is immersed in hexane. In order to correspond closely to the synthesized colloidal particles, we also assume that just outside the heterodimer there is a 2 nm shell of OAm surfactant (with a dielectric constant of 2.13), although this latter feature leads to very small spectral shifts relative to its exclusion.

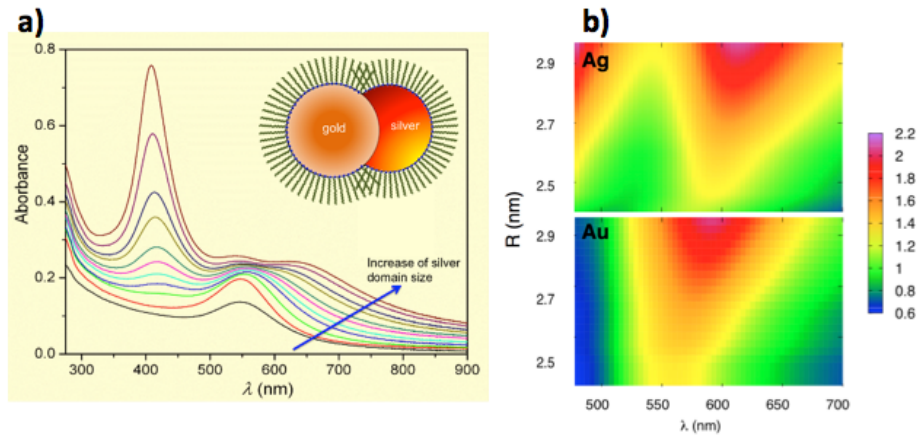


Figure 7: **a)** Absorption spectra of heterodimers with various silver domain sizes as controlled by reaction time. Longer reaction times correspond to larger silver domain sizes. **b)** Map of near-field intensity localized on the Ag domain (Top) and the Au domain (Bottom) as a function of wavelength and Ag domain size calculated using DDA in conjunction with a permittivity model that accounts for quantum size effects and interfacial modifications to the permittivity. Due to the interactions between the heterogeneous domains, the optical properties of the domains are a function of the silver domain size. This leads to the emergence of the CTP behavior, which can be seen by surprisingly large near-field enhancement on Ag and Au at long (550-700 nm) wavelengths. Reproduced with permission from Ref. 3.

Correction (i) mentioned in the preceding paragraph accounts for enhanced electron damping due to particle sizes becoming less than the classical mean free path of the conduction electrons. In applying it, we use a generalization of the usual size correction suggested by Liu and Guyot-Sionnest for metals that are interfaced with one another<sup>55</sup>. This correction accounts for the importance of electron scattering and other damping effects at the various interfaces between materials  $X$  and  $Y$  with parameters  $A_{X,Y}$ . The dielectric constant in a region occupied by Au involves a contribution from electrons scattering at the Au-surfactant interface, (quantified by parameter  $A_{Au,s}$ ), as well as a contribution from electrons scattering from the Au side of the Au/Ag interface, (quantified by parameter  $A_{Au,Ag}$ ). Similarly, the dielectric constant in a region occupied by Ag involves parameters  $A_{Ag,s}$  and  $A_{Ag,Au}$  reflecting electrons in Ag scattering at the Ag-surfactant and Ag/Au interfaces. It turns out that  $A_{Au,s}$ ,  $A_{Ag,s}$ , as well as the conductivity parameters involved in correction (ii) can all be fixed by requiring that the calculated spectra for only Au present ( $t = 0$  s) and for when the Ag domain is dominant ( $t = 180$  s) is in accord with experiment. As a result, only the two metal interface parameters,  $A_{Au,Ag}$  and  $A_{Ag,Au}$ , are to be determined such that the calculated spectra can describe the experimentally measured spectra as the Ag nanodomain increases. Consistent with general expectations, all the  $A_{X,Y}$  parameters are found to be on the order of 1 or less and  $A_{Ag,Au} > A_{Au,Ag}$ . The difference between  $A_{Ag,Au}$  and  $A_{Au,Ag}$  reflects the increased tendency of electrons on the Ag side to interact with the metalmetal interface, which is consistent with the elementary expectations (i.e., Au is more electronegative than Ag). Electronic structure calculations also support this argument<sup>3</sup>.

DDA calculations that utilize material permittivities calculated using the model just described allows us to theoretically reproduce the remarkable observed spectral features of the heterodimers. In particular, results using this model show the unusual enhancement of PK2 and the emergence of the broad PK3 with increasing the size of the Ag domain. The modification of the electron density of the outermost metal layers accounting for the chemical interactions with the surfactant layer (correction (ii)) leads to the appropriate red-



shifts of the SPR peaks. Introducing quantum size effects (correction (i)) both broadens and helps to correct the relative intensities of the SPR absorption peaks. Using this model, PK1 at 180 s has a fwhm of 50 nm in agreement with the experimental line width, while PK2 at 0 s has a fwhm of 60 nm and is within 10 nm of the experimental line width. At 180 s, PK2 and PK3 are 40% as intense as PK1 in the experimental spectrum. The calculated spectra with corrections (i) and (ii) find PK2 and PK3 to be 30% as intense as PK1 at 180 s, whereas without correction, PK2 and PK3 are 20% as intense as PK1. For the larger Ag nanodomains, the model also allows us to attribute PK3 to a charge transfer plasmon (CTP). The conditions for a CTP require conductive overlap of different metal domains, and the intensity of the CTP is larger when there is close matching of the static conductivity of the domains, that is, when  $(\sigma_{Au,0})/(\sigma_{Ag,0}) \approx 1$ , where the static conductivity is given by  $\sigma_{X,0} = (\omega_X^2)/(4\pi\gamma_X)^5$ . This ratio for the static conductivity of Au and Ag is  $\sim 0.32$  when bulk values of  $\gamma_X$  and  $\omega_X$  are used compared to 1.23 in the size-corrected model. Hence, quantum size effects and chemical interactions in this case create a stronger condition for CTP resonances in the interfaced heterodimers and the synergy of these effects gives rise to broadband absorption. Calculations with a fixed orientation along the interparticle axis (i.e., longitudinal axis) of the interfaced AuAg heterodimers resulted in an absorption spectrum with two intense peaks at positions close to PK1 and PK3<sup>3</sup>. Both longitudinal absorption peaks are broad and the absorption cross section, even at the peak valley position (approximately 480 to 500 nm), is much larger than the absorption cross-section of the corresponding pure Au nanoparticle. The positions of both longitudinal peaks red shift and their intensities increase as the Ag domain increases in size. The calculated near-field electric field distribution shows that the longitudinal peak at the shorter wavelength essentially originates from the SPR of the Ag domain<sup>3</sup>. The peak at the longer wavelength is ascribed to the CTP where charge oscillates between the Au and Ag domains, which should have only a longitudinal contribution<sup>5,7,8,17,48,49</sup>. Calculations along the transverse axis (i.e., the orientation perpendicular to the interparticle axis) of the interfaced AuAg

heterodimers lead to the observation of two absorption peaks at positions that are consistent with the characteristic SPR peaks of Au and Ag nanospheres<sup>3</sup>. As the size of the Ag domain increases the absorption cross section at the position of the Ag SPR increases accordingly while the absorption cross section at the position of the Au SPR diminishes slightly and slightly blue shifts. Although the formation of Au/Ag interface in an AuAg heterodimer does not significantly influence the transverse absorption cross section at wavelengths  $> 500$  nm, there is evidence that for larger silver particle sizes, PK2 results from transverse surface charge oscillations on both Au and the Ag surfaces<sup>3</sup>. The comparable near field intensity on the surfaces of both Au and Ag domains in the interfaced Au Ag heterodimer at wavelengths  $> 500$  nm indicates a cooperative behavior of electrons in Ag and Au, with PK3 showing CTP character. As a result, contributions of SPRs in both Au and Ag account for the broad absorption peaks (PK2 and PK3) of the interfaced AuAg heterodimers, while PK1 originates mainly from the Ag domains including both longitudinal and transverse SPR components with comparable contributions. The PK2 also includes both longitudinal and transverse SPR components and the increase in intensity of PK2 along with the growth of the Ag domains mainly originates from the longitudinal SPR component. The PK3 is dominated by the longitudinal SPR component. In summary, interfaced AuAg heterodimers in the quantum size regime with tunable domain sizes have been successfully synthesized through the asymmetric epitaxial overgrowth of Ag on partially passivated Au nanoparticles. The heterodimers support remarkable SPR modes including an unusually intense mode in the spectral region of the characteristic Au SPR and a broad mode that extends into near-infrared wavelengths. This behavior results from the synergistic interplay of the chemical interactions between the metal domains and the surfactant and quantum size effects. Calculations reveal that the SPRs in either Au or Ag domains exhibit broadband (400-900 nm) absorption, making them a possible class of photocatalysts with efficient utilization of visible light and high surface area associated with their small sizes<sup>57,58</sup>.

### 3.4 Perspective on the Horizon of Health Applications of Hybrid Nanostructures

Having now described some interesting phenomenology that has recently been discovered in hybrid nanostructures, and the theoretical tools capable of elucidating these phenomena, we now turn to what we believe are particularly compelling opportunities for optical nanostructures to make an impact for several health applications.

The ultimate realization of control over optical energy and information flow at nanoscale and molecular dimensions in terms of health applications is the ability to manipulate and observe sub-cellular structures and processes using light. In particular, we believe that precise control over biochemical reactions using light can be achieved with great implications for advancing therapeutic capabilities, and that construction of reliable *in vivo* optical systems can be achieved with great implications for advancing both therapeutic and diagnostic capabilities. As an example of the former, we will discuss potential opportunities for advancing the paradigm of photodynamic therapy. As an example of the latter, we will discuss recent advances and future opportunities for developing *in vivo* light sources such as intracellular lasers.

### 3.5 Photodynamic Therapy

Photodynamic therapy (PDT) is a form of therapy in which some light sensitive molecules, called photosensitizers, are targeted to a specific area or subset of tissues and then exposed to light. Activation of the photosensitizers by light leads to the generation of toxic or reactive oxygen species (ROS) in the targeted area that causes irreversible damage and death of the tissue<sup>59–62</sup>. This process is used currently for many diseases, from skin cancers, cancers of the esophagus, lungs, bladder, head and neck, to skin conditions like acne<sup>59,63–68</sup>. Photodynamic therapy is used both to cure and to manage the pain that these diseases bring<sup>69</sup>. PDT is used as a secondary or backup treatment of malignant tumors in the brain where removal of

part of the organ is required, and also in focal tumors where less than half of the tissue is affected<sup>60</sup>. Non cancer clinical indications include psoriasis, actinic keratosis, and infections such as periodontitis<sup>60</sup>.

Unlike photothermal therapy, where nanoparticles are excited by near-IR light which can penetrate relatively deeply into tissue, photosensitizers for PDT are generally activated with visible light, which has limited penetration depth in biological tissue<sup>60</sup>. This limits the application of PDT to superficial tissues, or to organs that accessible endoscopically like in the case of the bladder or esophagus<sup>60</sup>. The full range of uses of PDT is also limited due to the way light has to be sent to the targeted tissue, either by irradiation of the body or via fiber optics. Certainly one important challenge is the development of efficient modes of excitation for photosensitizers in deep tissue<sup>60</sup>. The use of up-conversion nanoparticles has been examined for this purpose<sup>60</sup>, which could allow conversion of maximally transmission near-IR photons into visible photons matched to photosensitizers.

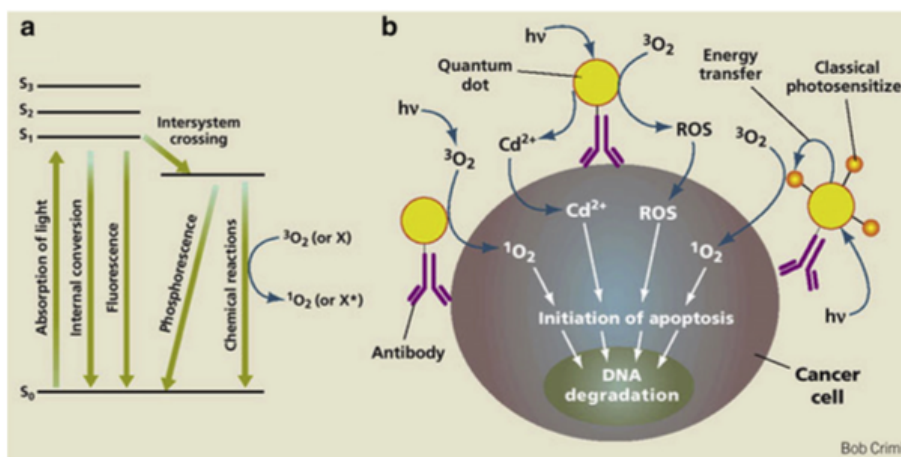


Figure 8: Schematic illustration of mechanisms of photodynamic therapy. **(a)** Illustrates the electronic structure of the photosensitizer. Photosensitizers in triplet excited states can interact with  $O_2$  to form ROS, which are various oxygen species in singlet excited-states. **(b)** Illustration of several ways PDT can initiate cell death. Hybrid nanostructures are already being investigated for PDT, including photosensitizers composed of quantum dot nanoparticles functionalized with small molecules to aid their selective uptake and binding. Illustration reproduced with permission from Ref. 60.

Future directions include increasing selectivity between type I and type II reactions, the

two methods by which singlet oxygen or reactive oxygen species are produced by the photosensitizer or photosensitizer nanoparticle (which is the main action that leads to cell death). In both Type I and II reactions, the photosensitizer is activated by light, generating a singlet excited state. The singlet excited state of the photosensitizer can radiatively relax, or it can undergo a spin conversion leading to a triplet excited state. Type I and Type II reactions are distinguished by the subsequent role of the photosensitizer in its triplet excited state in the generation of reactive oxygen species. In Type I reactions, the triplet photosensitizer species reacts with substrate molecules to form radicals which then react with ground state molecular oxygen to generate reactive oxygen species, including peroxides, superoxide anion radicals, and hydroxyl radicals, which can effect damage in the cell. In Type II reactions, the triplet state photosensitizer directly reacts with ground state oxygen to form singlet oxygen, which initiates cell death mechanisms and causes terminal damage to organelles. Several mechanisms of Type II reactions are illustrated in Figure 8. Other potential future directions include more specific targeting of the photosensitizers to diseased tissue, with less uptake by healthy tissue, and better light sources for irradiation and subsequent activation of the photosensitizers<sup>70-73</sup>. Another considerable challenge is to enhance the selectivity of ROS generation, and consequently, selectivity of the biochemical pathways that lead to cell death. A complementary challenge to selective generation of ROS generation is the precise, real-time detection of ROS concentration for elucidating the details of the relevant biochemical pathways<sup>74</sup>. The selective delivery of photosensitizer agents to malignant cells, while minimizing their uptake by normal healthy tissues, is also a considerable challenge. It is our view that these challenges will be addressed by recent and future advances and discoveries in nanoscience. Indeed, controlling the absorption window of photosensitizers, and controlling the selectivity of the ROS species they generate, may be enabled by the type of emergent plasmonic phenomena observed in hybrid metallic nanostructures<sup>3</sup>. The diversity of the challenges facing PDT demand solutions that combine multiple flexible and synergistic functionalities, which is a promising feature of systems involving hybrid nanostructures. Here,

we briefly review some of the recent developments in nanoscience that are advancing the paradigm of photodynamic therapy.

Nanoparticle platforms have been exploited because of their ability to transport hydrophobic drugs in the blood, their large surface areas which can be modified to have specific affinities, their ability to be taken up by various cell types, and their to controllably release drugs. Nanoparticles in PDT may be classified as passive or active, where the former do not participate in the excitation of the photosensitizers, whereas the latter do play a role in the excitation of photosensitizers or oxygen species. Within the passive group, the nanoparticles can be divided into another two groups, biodegradable polymer-based nanoparticles or non-polymer-based nanoparticles<sup>60</sup>. The active nanoparticles are divided into groups based on how they activate the photosensitizers and by which mechanisms of action they exploit<sup>60</sup>. Photosensitizer nanoparticles that can replace the need for small-molecule photosensitizers comprise the first class of active nanoparticles. In this class, the nanoparticle is made of a semiconducting material which can itself generate singlet oxygen. So far, the efficiency of singlet oxygen generation through this method is lower than through the use of small molecule photosensitizers. To increase the yield of singlet oxygen produced, small molecule photosensitizers may be adhered to the surface of the nanoparticle; however, these conjugates have low water solubility<sup>75</sup>. This problem may be solved with the used of liposomes or some other micelle that allows for delivery to the targeted cells.

Self-lighting nanoparticles are nanoparticle that act as the light source for photosensitizers that comprise a second group of active nanoparticles. Persistent luminescence nanoparticles may be attached to photosensitizers<sup>72</sup>. Irradiation of these hybrids causes the nanoparticles to luminesce, thereby activating the photosensitizers to generate ROS. This strategy has been used in conjunction with radiation therapy for cancer treatment, in order to reduce the exposure to radiation<sup>72</sup>.

Upconverting nanoparticles have been used to try to overcome the limited penetration depth of visible light required to activate photosensitizers. The nanoparticles are able to

absorb multiple low energy (e.g. near-IR) photons that are maximally transmissive in tissue and emit higher-energy (e.g. visible) photons capable of exciting the photosensitizers that they are conjugated with<sup>76</sup>. This allows photodynamic therapy to be used for indications where the targeted tissues are not necessarily on the surface of the skin or otherwise superficial.

### 3.6 *in vivo* light sources

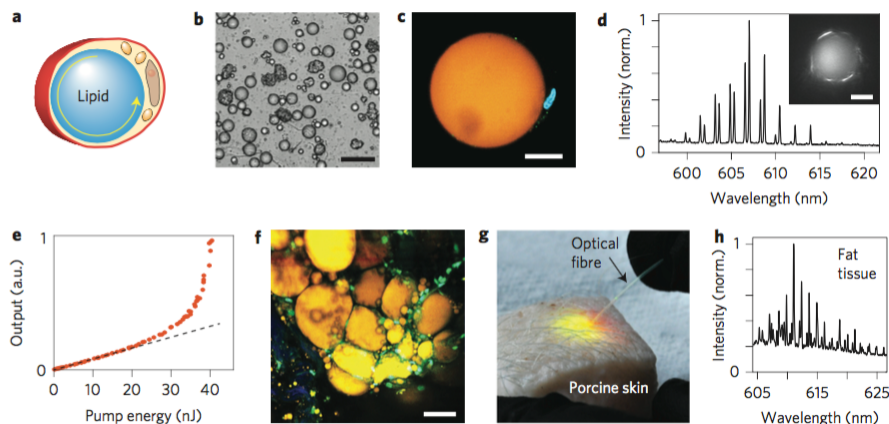


Figure 9: Demonstration of intracellular lasers operating in fat cells. **(a)** Schematic of a typical adipocyte (fat cell) with a spherical lipid droplet. **(b)** Microscope images of individual adipocytes. **(c)** Confocal image of an adipocyte containing a large lipid droplet. **(d)** Spectrum from a  $45\ \mu\text{m}$  adipocyte above lasing threshold, showing typical WGM spectral peaks. **(e)** Output energy as a function of pump energy of the intracellular laser. **(f)** Two-photon confocal image of adipocytes in fat tissue after inclusion of gain medium. **(g)** Intracellular laser emission from within tissue. The pump laser is fibre-optically guided into the adipocytes. **(h)** Spectrum of the intracellular laser. The peak positions depends critically upon the size and refractive index of the lipid sphere. Figure reproduced with permission from Ref. 77.

The ability to construct optical systems that have truly sub-cellular size is another promising application of nanophotonics, and the multiple functionalities required by such a system (light emission, focusing and collection of light) will no doubt rely on the careful engineering of hybrid nanostructures. One can imagine many health applications of such a system. For example, *in vivo* optical systems could be used in conjunction with PDT strategies to enable more effective delivery of light to deep tissues. They could also be used in *in vivo* spec-

troscopies to precisely probe biochemical events. Here we describe one particularly exciting recent development which is part of this puzzle, the generation of so-called intracellular microlasers<sup>77</sup>. These devices are in themselves hybrid nano (or micro) structures, consisting of a spherical dielectric nano- or microparticle in conjunction with a gain medium, which may be a small molecule dye, a quantum dot, etc. The gain medium can be located in the core of the dielectric nano- or microparticle, or it may decorate the surface of the dielectric particle<sup>77</sup>

Recently, Humar and Yun have described an effective approach for generating *in vivo* lasers by exploiting intracellular whispering-gallery modes (WGM) as the optical resonance of the laser<sup>77</sup>. A WGM is produced when light circulating in a spherical particle is trapped due to total internal reflection. Humar and Yun demonstrated that adipocytes (fat cells) can naturally support WGM via their micron-scale spherical lipid droplets<sup>77</sup>. Gain media can be introduced into the adipocyte, either inside the lipid droplet or into the region surrounding the droplet, to allow lasing. They showed that upon pulsed excitation, lipid droplets larger than  $7\text{ }\mu\text{m}$  experienced lasing. Importantly, the cells were not damaged by the laser emission or by the minimal heating ( $< 1^\circ$ ) observed. Humar and Yun also demonstrated the use of solid microspheres, which can be engulfed by certain cells, as the optical resonators of the laser<sup>77</sup>. The use of solid micro- or nanoparticles as the resonator offers greater control over the WGM spectrum and the quality factor of the resonator, which allows the intracellular lasers based on solid particles to have lower lasing thresholds and greater spectral selectivity<sup>77</sup>.

Opportunities exist to advance these light sources by decreasing the size of the optical resonators and increasing the biocompatibility of the structure<sup>77</sup>. By increasing the biocompatibility, this technology could be used in the future for minimally invasive treatments of cancer, for precise drug delivery without the use of needles, and for selectively inducing blood clotting.

Plasmonic particles are particularly small optical resonators that could be leveraged to decrease the size of *in vivo* coherent light sources. A nanoscale laser that utilizes plasmonic



resonators is called a spaser<sup>78</sup>. In the way that a laser can generate a simulated emission of coherent photons, a spaser can generate stimulated emission of surface plasmons via a resonating metallic nanoparticle adjacent to a gain medium<sup>78</sup>. Such devices have been realized in hybrid nanoparticles consisting of a gold core and a dye-doped silica shell. With further development of this technology, these nano-lasers could be leveraged to control the flux of optical energy in cellular and sub-cellular environments as required by photodynamic and photothermal therapies. Beyond these two light-driven therapies, *in vivo* light sources also have the potential to considerably increase the safety of surgery. The control of blood clotting is a major concern in surgery, and adverse interactions with anticoagulant drugs is a leading cause of complications and death associated with surgery<sup>79</sup>. Hybrid nanostructures are being investigated that can controllably release binding agents that block the effect of anticoagulants, as well as agents that restore the effect of anticoagulants, upon activation by light<sup>79</sup>. The ability to tune the optical response of these hybrid nanoparticles, and the ability to precisely deliver the appropriate optical stimulus, are both key to the development of this technology.

## 4 Concluding Remarks

There is indeed a great deal of diversity in the optical response of nanoelements and nanohybrids, and a great deal of diversity in the types of applications that can exploit them. Although a single chapter cannot capture even a fraction of this diversity, we have tried to give a glimpse of it by highlighting some of our own contributions, and some of the work that motivated those contributions. In doing so, we hope to inspire the reader to look deeper into the field. We have also described several important theoretical and computational approaches which can be used to explore the vast field of nanophotonics, and which can be brought to bear in designing nanoelements and nanohybrids for a variety of applications. Finally, we have tried to articulate, by way of discussing two emerging technologies (photo-

dynamic therapy and *in vivo* lasers), a broader vision for how we believe optical nanohybrids will play a role in transformative health applications in the future.

## References

- (1) Gray, S. K. Theory and Modeling of Plasmonic Structures. *J. Phys. Chem. C* **2013**, *117*, 1983–1994.
- (2) Bohren, C. F.; Huffman, D. R. *Absorption and Scattering of Light by Small Particles*; John Wiley and Sons, 1998.
- (3) Sun, Y.; Foley IV, J. J.; Peng, S.; Li, Z.; K., G. S. Interfaced metal heterodimers in the quantum size regime. *Nano Lett.* **2013**, *13*, 3958–3964.
- (4) Savage, K. J.; Hawkeye, M. M.; Esteban, R.; Borisov, A. G.; Aizpurua, J.; Baumberg, J. J. Revealing the quantum regime in tunnelling plasmonics. *Nature* **2012**, *491*, 574577.
- (5) Esteban, R.; Borisov, A. G.; Nordlander, P.; Aizpurua, J. Bridging quantum and classical plasmonics with a quantum-corrected model. *Nat. Commun.* **2012**, *3*, 825.
- (6) Scholl, J. A.; García-Etxarri, A.; Koh, A. L.; Dionne, J. A. Observation of Quantum Tunneling between Two Plasmonic Nanoparticles. *Nano Lett.* **2013**, *13*, 564569.
- (7) Pérez-González, O.; Zabala, N.; Aizpurua, J. Optical characterization of charge transfer and bonding dimer plasmons in linked interparticle gaps. *New J. Phys.* **2011**, *13*, 083013.
- (8) Zuloaga, J.; Prodan, E.; Nordlander, P. Quantum Description of the Plasmon Resonances of a Nanoparticle Dimer. *Nano Lett.* **2009**, *9*, 887891.
- (9) Foley IV, J. J.; McMahon, J. M.; Schatz, G. C.; Harutyunyan, H.; Wiederrecht, G. P.; Gray, S. K. *ACS Photonics* **2014**, *1*, 739–745.

- (10) Taflove, A.; Hagness, S. C. *Computational Electrodynamics: the finite-difference time-domain method*; Artech, 2000.
- (11) Oskooi, A. F.; Roundy, D.; Ibanescu, M.; Bermel, P.; Joannopoulos, J. D.; Johnson, S. G. MEEP: A flexible free-software package for electromagnetic simulations by the FDTD method. *Comp. Phys. Comm.* **2010**, *181*, 687702.
- (12) Yeh, P. *Optical waves in layered media*; Wiley, 2005.
- (13) Draine, B. T.; Flatau, P. J. Discrete-dipole approximation for scattering calculations. *J. Opt. Soc. Am. A* **1994**, *11*, 1491–1499.
- (14) McMahon, J. M. Topics in Theoretical and Computational Nanoscience: From Controlling Light at the Nanoscale to Calculating Quantum Effects with Classical Electrodynamics. Ph.D. thesis, Northwestern University, 2011.
- (15) Brown, L. V.; Sobhani, H.; Lassiter, J. B.; Nordlander, P.; Halas, N. J. Heterodimers: Plasmonic Properties of Mismatched Nanoparticle Pairs. *ACS Nano* **2010**, *4*, 819–832.
- (16) Cole, J. R.; Halas, N. J. Optimized plasmonic nanoparticle distributions for solar spectrum harvesting. *Appl. Phys. Lett.* **2006**, *89*, 153120.
- (17) Lassiter, J. B.; Aizpurua, J.; Hernandez, L. I.; Brandl, D. W.; Romero, I.; Lal, S.; Hafner, J. H.; Nordlander, P.; Halas, N. J. Close Encounters between Two Nanoshells. *Nano Lett.* **2008**, *8*, 12121218.
- (18) Li, Z.; Foley IV, J. J.; Peng, S.; Sun, C.-J.; Ren, Y.; Wiederrecht, G. P.; Gray, S. K.; Sun, Y. Reversible Modulation of Surface Plasmons in Gold Nanoparticles Enabled by Surface Redox Chemistry. *Angew. Chem.* **2015**, *127*, 9076–9079.
- (19) Ben-Adballah, P.; Ni, B. Single-defect Bragg stacks for high-power narrow-band thermal emission. *J. Appl. Phys* **2005**, *97*, 104910.

- (20) Lee, B. J.; Zhang, Z. M. Design and fabrication of planar multilayer structures with coherent thermal emission characteristics. *J. Appl. Phys* **2006**, *100*, 063529.
- (21) Chen, Y.; Zhang, D.; Zhu, L.; Fu, Q.; Wang, R.; Wang, P.; Ming, H.; Badugu, R.; Lakowicz, J. R. Effect of metal film thickness on Tamm plasmon-coupled emission. *Phys. Chem. Chem. Phys.* **2014**, *16*, 25523–25530.
- (22) Griesing, S.; Englisch, A.; Hartmann, U. Refractive and reflective behavior of polymer prisms used for surface plasmon guidance. *Opt. Lett.* **2008**, *33*, 575577.
- (23) Kitazawa, T.; Miyanishi, S.; Murakami, Y.; Kojima, K.; Takahashi, A. Refraction of surface plasmon polaritons at Au-Al boundaries observed by near-field optical microscopy. *Phys. Rev. B* **2008**, *77*, 193404.
- (24) Novotny, L.; Hecht, B. *Principles of nano-optics*, 2nd ed.; Cambridge University Press, 2012.
- (25) Maier, S. M. *Plasmonics: Fundamentals and applications*; Springer, 2007.
- (26) Lal, S.; Clare, S. E.; Halas, N. J. Nanoshell-enabled photothermal cancer therapy: impending clinical impact. *Acc. Chem. Res.* **2008**, *41*, 1842–1851.
- (27) Huang, X.; El-Sayed, M. A. Plasmonic photo-thermal therapy (PPTT). *Alexandria Journal of Medicine* **2011**, *47*, 1–9.
- (28) Averrit, R. D.; Westcott, S. L.; Halas, N. J. Linear optical properties of gold nanoshells. *J. Opt. Soc. Am. B* **1999**, *16*, 1824–1832.
- (29) Raether, H. *Surface Plasmons on Smooth and Rough Surfaces and on Gratings*; Springer-Verlag, 1988.
- (30) Datas, A.; Hirashima, D.; Hanamura, K. FDTD simulation of near-field radiative heat transfer between thin films supporting surface phonon polaritons: Lessons learned. *J. Therm. Sci. Tech.* **2013**, *8*, 91–105.

- (31) Caldwell, J. D.; Lindsay, L.; Giannini, V.; Vurgaftman, I.; Reinecke, T. L.; Maier, S. A.; Glembocki, O. J. Low-loss, infrared and terahertz nanophotonics using surface phonon polaritons. *Nanophotonics* **2014**, *4*, 2192.
- (32) Wendler, L.; Haupt, R. An improved virtual mode theory of ATR Experiments of Surface Polaritons. *Phys. Stat. Sol. b* **1987**, *143*, 131–147.
- (33) Atwater, H. A.; Polman, A. Plasmonics for improved photovoltaic devices. *Nature Mater.* **2010**, *9*, 205–213.
- (34) Foley IV, J. J.; Harutyunyan, H.; Rosenmann, D.; Divan, R.; Wiederrecht, G. P.; Gray, S. K. When are Surface Plasmon Polaritons Excited in the Kretschmann-Raether Configuration? *Sci. Rep.* **2015**, *5*, 09929.
- (35) Driessen, E. F. C.; de Dood, M. J. A. The perfect absorber. *Appl. Phys. Lett.* **2009**, *94*, 171109.
- (36) Kats, M. A.; Sharma, D.; Lin, J.; Genevet, P.; Blanchard, R.; Yang, Z.; Qazilbash, M. M.; Basov, D. N.; Ramanathan, S.; Capasso, F. Ultra-thin perfect absorber employing a tunable phase change material. *App. Phys. Lett.* **2012**, *101*, 221101.
- (37) Kats, M. A.; Blachard, R.; Genevet, P.; Capasso, F. Nanometer optical coatings based on strong interference effects in highly absorbing media. *Nat. Mat.* **2013**, *12*, 20–24.
- (38) Patching, S. G. Surface plasmon resonance spectroscopy for charecterisation of membrane protein-ligand interactions and its potential for drug discovery. *Biochim. Biophys. Acta* **2014**, *1838*, 43–55.
- (39) Lumerical Solutions, Inc., <http://www.lumerical.com/tcad-products/mode/>.
- (40) Yurkin, M. A.; Min, M.; Hoekstra, A. G. Applicaton of the discrete dipole approximation to very large refractive indices: Filtered doupdled dipoles revived. *Phys. Rev. E* **2010**, *82*, 036703.

- (41) Loke, V. L. Y.; Menguc, M. P. Surface waves and atomic force microscope probe-particle near-field coupling: discrete dipole approximation with surface interaction. *J. Opt. Soc. Am. A* **2010**, *27*, 2293–2303.
- (42) Edalatpour, S.; Francoeur, M. The thermal discrete dipole approximation (T-DDA) for near-field radiative heat transfer simulations in three-dimensional arbitrary geometries. *J. Quant. Spect. Radiat. Transf.* **2015**, *133*, 364–373.
- (43) Lezec, H. J.; Dionne, J. A.; Atwater, H. A. Negative refraction at visible frequencies. *Science* **2007**, *316*, 430432.
- (44) Schermelleh, L.; Heintzmann, R.; Leonhardt, H. A guide to super-resolution fluorescence microscopy. *J. Cell. Biol.* **2010**, *190*, 165–175.
- (45) Scholl, J. A.; Koh, A. L.; Dionne, J. A. Quantum plasmon resonances of individual metallic nanoparticles. *Nature* **2012**, *483*, 421–427.
- (46) Peng, S.; McMahon, J. M.; Schatz, G. C.; Gray, S. K.; Sun, Y. Reversing the size-dependence of surface plasmon resonances. *Proc. Natl. Acad. Sci. U.S.A.* **2010**, *107*, 1453014534.
- (47) Atay, T.; Song, J.-H.; Nurmikko, A. V. Strongly Interacting Plasmon Nanoparticle Pairs: From Dipole-Dipole Interaction to Conductively Coupled Regime. *Nano Lett.* **2004**, *4*, 16271631.
- (48) Song, P.; Nordlander, P.; Gao, S. Quantum mechanical study of the coupling of plasmon excitations to atomic-scale electron transport. *J. Chem. Phys.* **2011**, *134*, 074701.
- (49) Zhao, K.; Troparevsky, M. C.; Xiao, D.; Eguiluz, A. G.; Zhang, Z. Electronic Coupling and Optimal Gap Size between Two Metal Nanoparticles. *Phys. Rev. Lett.* **2009**, *102*, 186804.

- (50) Johnson, P. B.; Christy, R. W. Optical constants of noble metals. *Phys. Rev. B* **1972**, *6*, 4370.
- (51) Flatau, P. J.; Draine, B. T. *Opt. Exp.* **2012**, *20*, 12471252.
- (52) Genzel, L.; Martin, T. P.; Kreibig, U. Dielectric function and plasma resonances of small metal particles. *Z. Phys. B* **1975**, *21*, 339346.
- (53) Kraus, W. A.; Schatz, G. C. Plasmon resonance broadening in small metal particles. *J. Chem. Phys.* **1983**, *79*, 61306139.
- (54) Coronado, E. A.; Schatz, G. C. Surface plasmon broadening for arbitrary shape nanoparticles: A geometrical probability approach. *J. Chem. Phys.* **2003**, *119*, 39263924.
- (55) Liu, M.; Guyot-Sionnest, P. Synthesis and Optical Characterization of Au/Ag Core/Shell Nanorods. *J. Phys. Chem. B* **2004**, *108*, 58825888.
- (56) Sun, Y.; Gray, S. K.; Peng, S. Surface chemistry: a non-negligible parameter in determining optical properties of small colloidal metal nanoparticles. *Phys. Chem. Chem. Phys.* **2011**, *13*, 1181411826.
- (57) Christopher, P.; Xin, H.; Linic, S. Visible-light-enhanced catalytic oxidation reactions on plasmonic silver nanostructures. *Nature Chem.* **2011**, *3*, 467472.
- (58) Linic, S.; Christopher, P.; Ingram, D. B. Plasmonic-metal nanostructures for efficient conversion of solar to chemical energy. *Nat. Mater.* **2011**, *10*, 911921.
- (59) Triesscheijn, M.; Baas, P.; Schellens, J. H.; Stewart, F. A. Photodynamic therapy in oncology. *Oncologist* **2006**, *11*, 1034–1044.
- (60) Chatterjee, D. K.; Fong, L. S.; Zhang, Y. Nanoparticles in photodynamic therapy: An emerging paradigm. *Adv. Drug Deliv. Rev.* **2008**, *60*, 1627–1637.

- (61) Trachootham, D.; Alexandre, J.; Huang, P. Targeting cancer cells by ROS-mediated mechanisms: a radical therapeutic approach? *Nat. Rev. Drug. Discov.* **2009**, *8*, 579–591.
- (62) Dolmans, D. E. J. G. J.; Fukumura, D.; Jain, R. K. Photodynamic therapy for cancer. *Nat. Rev. Cancer* **2003**, *3*, 380–387.
- (63) Dougherty, T. J.; Kaufman, J. E.; Goldfarb, A.; Weishaupt, K. R.; Boyle, D.; Mittleman, A. Photoradiation therapy for the treatment of malignant tumors. *Cancer Res.* **1978**, *38*, 2628–2635.
- (64) Kato, H. Photodynamic therapy for lung cancer – a review of 19 years’ experience. *J. Photochem. Photobiol.* **1998**, *B42*, 96–99.
- (65) Hur, C.; Nishioka, N. S.; Gazelle, G. S. Cost-effectiveness of photodynamic therapy for treatment of Barrett’s esophagus with high grade dysplasia. *Dig. Dis. Sci.* **2003**, *48*, 1273–1283.
- (66) Skyrme, R. J.; French, A. J.; Datta, S. N.; Allman, R.; Mason, M.; Matthews, P. A phase-1 study of sequential mitomycin C and 5-aminolaevulinic acid-mediated photodynamic therapy in recurrent superficial bladder carcinoma. *BJU Int.* **2005**, *95*, 1206–1210.
- (67) Schuller, D. E.; McCaughan Jr., J. S.; Rock, R. P. Photodynamic therapy in head and neck cancer. *Arch. Otolaryngol.* **1985**, *111*, 351–355.
- (68) Rhodes, L. E.; de Rie, M.; Enstrom, Y.; Groves, R.; Morken, T.; Goulden, V.; Wong, G. A.; Grob, J. J.; Varma, S.; Wolf, P. Photodynamic therapy using topical methyl aminolevulinate vs surgery for nodular basal cell carcinoma: results of a multi-center randomized prospective trial. *Arch. Dermatol.* **2004**, *140*, 17–23.



- (69) Hopper, C.; Niziol, C.; Sidhu, M. The cost-effectiveness of Foscan mediated photodynamic therapy (Foscan-PDT) compared with extensive palliative surgery and palliative chemotherapy for patients with advanced head and neck cancer in the UK. *Oral Oncol.* **2004**, *40*, 372–382.
- (70) Foote, C. Definition of type I and type II photosensitized oxidation. *Photochem. Photobiol.* **1991**, *54*, 659.
- (71) Niedre, M.; Patterson, M. S.; Wilson, B. C. Direct near-infrared luminescence detection of singlet oxygen generated by photodynamic therapy in cells in vitro and tissues in vivo. *Photochem. Photobiol.* **2002**, *75*, 382–391.
- (72) Chen, W.; Zhang, J. Using nanoparticles to radiation and photodynamic therapies for cancer treatment. *J. Nanosci. Nanotechnology* **2006**, *6*, 1159–1166.
- (73) Konan-Kouakou, Y. N.; Boch, R.; Gurny, R.; Allemann, E. In vitro and in vivo activities of verteporfin-loaded nanoparticles. *J. Control. Release* **2005**, *103*, 83–91.
- (74) Dickinson, B. C.; Chang, C. J. Chemistry and biology of reactive oxygen species in signaling or stress responses. *Nat. Chem. Biol.* **2011**, *7*, 504–511.
- (75) Samia, A. C.; Chen, X.; Burda, C. Semiconductor quantum dots for photodynamic therapy. *J. Am. Chem. Soc.* **2003**, *125*, 15736–15737.
- (76) Boyer, J. C.; Vetrone, F.; Cuccia, L. A.; Capobianco, J. A. Synthesis of colloidal upconverting NaYF<sub>4</sub> nanocrystals doped with Er<sup>3+</sup>, Yb<sup>3+</sup> and Tm<sup>3+</sup>, Yb<sup>3+</sup> via thermal decomposition of lanthanide trifluoroacetate precursors. *J. Am. Chem. Soc.* **2006**, *128*, 7444–7445.
- (77) Humar, M.; Yun, S. H. Intracellular microlasers. *Nature Photon.* **2015**, *9*, 572–576.
- (78) Noginov, M. A.; Zhu, G.; Belgrave, A. M.; Bakker, R.; Shalae, V.; Narimanov, E. E.;

- Stout, S.; Herz, E.; Suteewong, T.; Wiesner, U. Demonstration of a spaser-based nanolaser. *Nature* **2009**, *460*, 1110–1112.
- (79) de Puig, H.; Rius, A. C.; Flemister, D.; Baxamusa, S. H.; Hamad-Schifferli, K. Slective Light-Triggered Release of DNA from Gold Nanorods Switches Blood Clotting On and Off. *PLOS ONE* **2013**, *8*, e68511.